



High-temperature stable anatase-type TiO₂ nanotube arrays: A study of the structure–activity relationship



Hamed Eskandarloo^{a,b,*}, Mazdak Hashempour^a, Antonello Vincenzo^a, Silvia Franz^a,
Alireza Badiei^b, Mohammad A. Behnajady^c, Massimiliano Bestetti^a

^a Department of Chemistry, Materials and Chemical Engineering “Giulio Natta”, Politecnico di Milano, Milano, Italy

^b School of Chemistry, College of Science, University of Tehran, Tehran, Iran

^c Department of Chemistry, Tabriz Branch, Islamic Azad University, Tabriz, Iran

ARTICLE INFO

Article history:

Received 11 August 2015

Received in revised form

24 November 2015

Accepted 27 November 2015

Available online 10 December 2015

Keywords:

Anodic oxidation

Titania nanotubes

Anatase

Noble metal deposition

Photoelectrocatalytic activity

ABSTRACT

Anatase-type TiO₂ nanotube arrays (TiO₂-NTAs) were grown on Ti foil by anodic oxidation in CH₃COOH/NH₄F solutions followed by thermal treatment. The surface of TiO₂-NTAs was further decorated by palladium and silver metal clusters through a chemical-reduction method and its photocatalytic activity was tested by investigating the degradation of p-nitrophenol (PNP) in aqueous solution under visible-light irradiation and electrical polarization. The effects of preparation variables both on microstructural properties of samples and photocatalytic activity were examined by using the 3D response surface and the 2D contour plots. The experimental investigations carried out by using XRD, SEM, HRTEM, EDS, XRF, ICP-AES, XPS, DRS, and PL, demonstrated a strong relation between the phase structure and the photocatalytic activity of TiO₂-NTAs. Titania nanotubes grown in acetic acid solution and thermally post-treated have stable anatase crystal structure, to a point that by performing annealing at 800 °C for 3 h, only the 35% of anatase transforms into rutile. Finally, it was shown that the TiO₂-NTAs decorated with Pd(0.72 wt%) and Ag(1.26 wt%) particles show higher photocatalytic activity compared with nanotubes modified with single metal particles. It is believed that the high photoactivity of TiO₂ nanotubes decorated with Pd–Ag heterostructures is due to the prolonged lifetimes of photogenerated electron–hole pairs. The possible mechanism for the enhanced photocatalytic activity is discussed in detail.

© 2015 Elsevier B.V. All rights reserved.

1. Introduction

Heterogeneous photocatalysis processes based on light irradiation of an oxide semiconductor, have received considerable attention for application in various fields [1]. When an oxide semiconductor absorbs photons with energy greater than the band-gap, valence electrons are promoted to the conduction band and leaving holes behind. The photogenerated electron–hole pairs can react directly or indirectly, through the mediation of radicals, with a number of species in aqueous solutions [2,3]. One of the main losses in the photocatalytic activity of oxide semiconductors is the fast recombination of electron–hole pairs, and an effective way to prevent such recombination is the deposition of noble metal clusters onto the semiconductor surface [4–7]. The metal clusters

act as electron scavenger at each metal–semiconductor contact region (Schottky barrier), reducing the recombination probability of photogenerated electron–hole pairs [4–7]. Moreover, noble metal particles with plasmon resonance in the UV and near-UV–vis light optical range, can harvest and transfer more light energy to the oxide semiconductor. This phenomenon leads to generate more electron–hole pairs and to an enhancement of photocatalytic activity [7–9]. In recent years, the co-deposition of two metal species onto the semiconductor surface, as more efficient electron scavenging system than the single metal deposition, has been proposed [10].

Among the oxide semiconductors, titanium dioxide (TiO₂) with anatase crystal structure is well known as an efficient photocatalyst [11]. In the majority of studies on photocatalysis, TiO₂ is utilized in form of powder dispersed in solution. However, the separation step of TiO₂ powders from slurry after photocatalytic treatment adds to the overall costs of the process [4]. Therefore, recent studies have focused on the use of TiO₂ layers immobilized on a support in order to avoid the powder separation step, the aggregation of catalyst particles during the photoreaction, and also the light intensity

* Corresponding author at: Department of Chemistry, Materials and Chemical Engineering “Giulio Natta”, Politecnico di Milano, Milano, Italy.

E-mail addresses: eskandarloo@ut.ac.ir, eskandarloo@gmail.com (H. Eskandarloo).

attenuation due to optical losses in the slurry, which cause over-all inefficiencies in the process. There are several techniques for preparation of the nanostructured TiO_2 immobilized on substrates. Among them, anodic oxidation followed by thermal treatment has attracted much attention due to its simplicity in operation and easy control in the direct growth of TiO_2 nanotube arrays (TiO_2 -NTAs) on Ti substrate [12,13]. Numerous studies describe the synthesis of TiO_2 -NTAs, however the electrochemical preparation of TiO_2 -NTAs with anatase crystal structure that is stable at high temperature has not yet been reported. The enhanced thermal stability is useful to improve the photocatalytic activity, because a higher level of crystallinity can be obtained by annealing titania at high temperatures without forming the rutile phase, which is responsible for the low photocatalytic activity of TiO_2 [11,14].

One of the aims of this study was the preparation of TiO_2 -NTAs with anatase crystal structure on Ti foil by anodic oxidation and thermal post-treatment, followed by chemical-deposition of Pd and Ag metallic clusters. An ultrasonic treatment after the anodization step was carried out to remove contaminants from the nanotubes surface to obtain an open tube morphology easily accessible to light irradiation and target molecules in photocatalytic reaction [15,16]. Moreover, as second aim, the photoelectrocatalytic activity was evaluated for the removal of PNP (p-nitrophenol) as a model organic pollutant from aqueous solutions under visible-light irradiation and electrical polarization as an external electric field affects the separation rate of the photogenerated electron–hole pairs [17].

The effects of operating variables, such as anodic oxidation voltage and time, annealing temperature and time, and Pd and Ag contents on structural properties of samples, as well as on their photoelectrocatalytic activity were optimized using the response surface methodology (RSM).

2. Materials and methods

2.1. Materials

Titanium foils with 99.6% purity (Ti grade 1, annealed, thickness 100 μm) were purchased from Ti-Shop.com. Hydrofluoric acid, sulfuric acid, ammonium fluoride, acetic acid, palladium chloride, silver nitrate, sodium borohydride, acetone, and p-nitrophenol, were all of analytical grade quality and purchased from Sigma–Aldrich.

2.2. Preparation of anatase-type TiO_2 -NTAs

Amorphous TiO_2 -NTAs were grown on Ti foil by anodic oxidation followed by ultrasonic treatment. Titanium foils were annealed at 400 $^\circ\text{C}$ for 6 h and pickled in aqueous solution of 2 M HF and 0.5 M H_2SO_4 to remove the thermal oxide. Then titanium foils were degreased by ultrasonic treatment in acetone, followed by rinsing in deionized water and finally dried with nitrogen gas flow. The anodic oxidation was carried out in a solution of CH_3COOH (con-

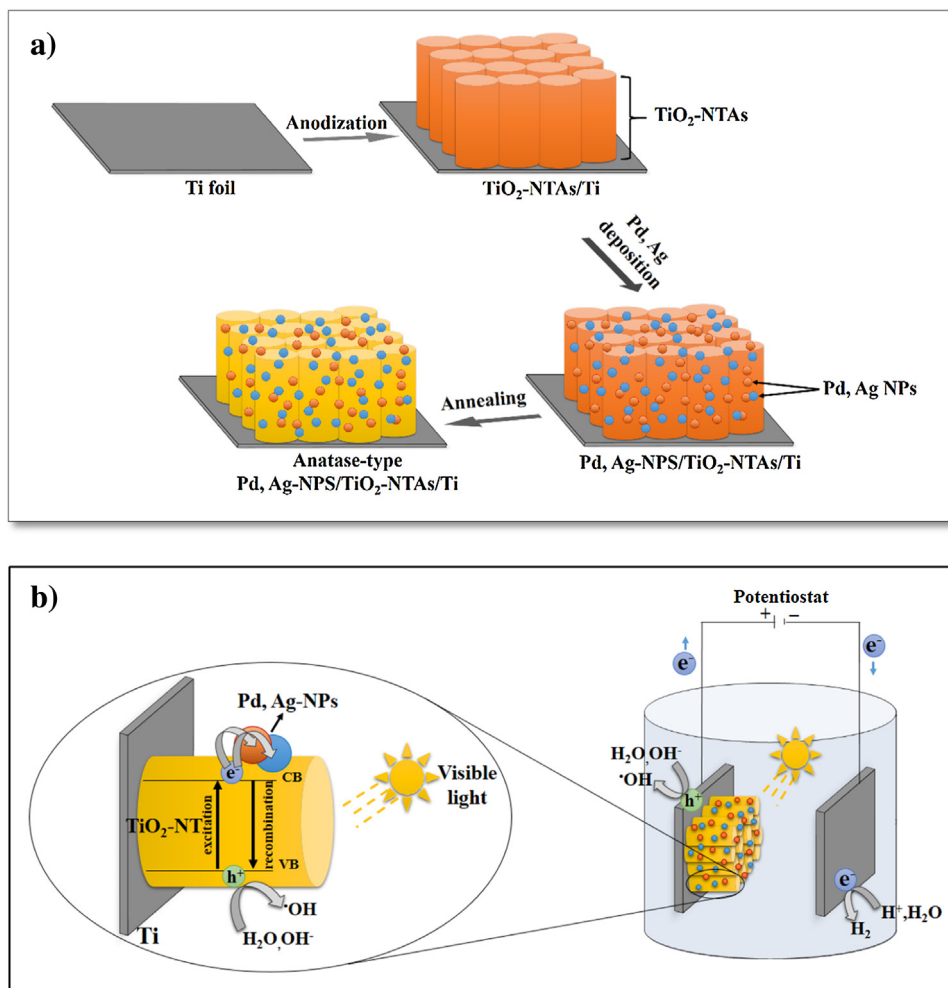


Fig. 1. Schematic illustration of (a) formation of anatase-type TiO_2 -NTAs and Pd, Ag deposition processes and (b) photoelectrochemical reaction system with the proposed mechanism of reaction scheme over Pd,Ag-NPs/ TiO_2 -NTAs under visible light irradiation.

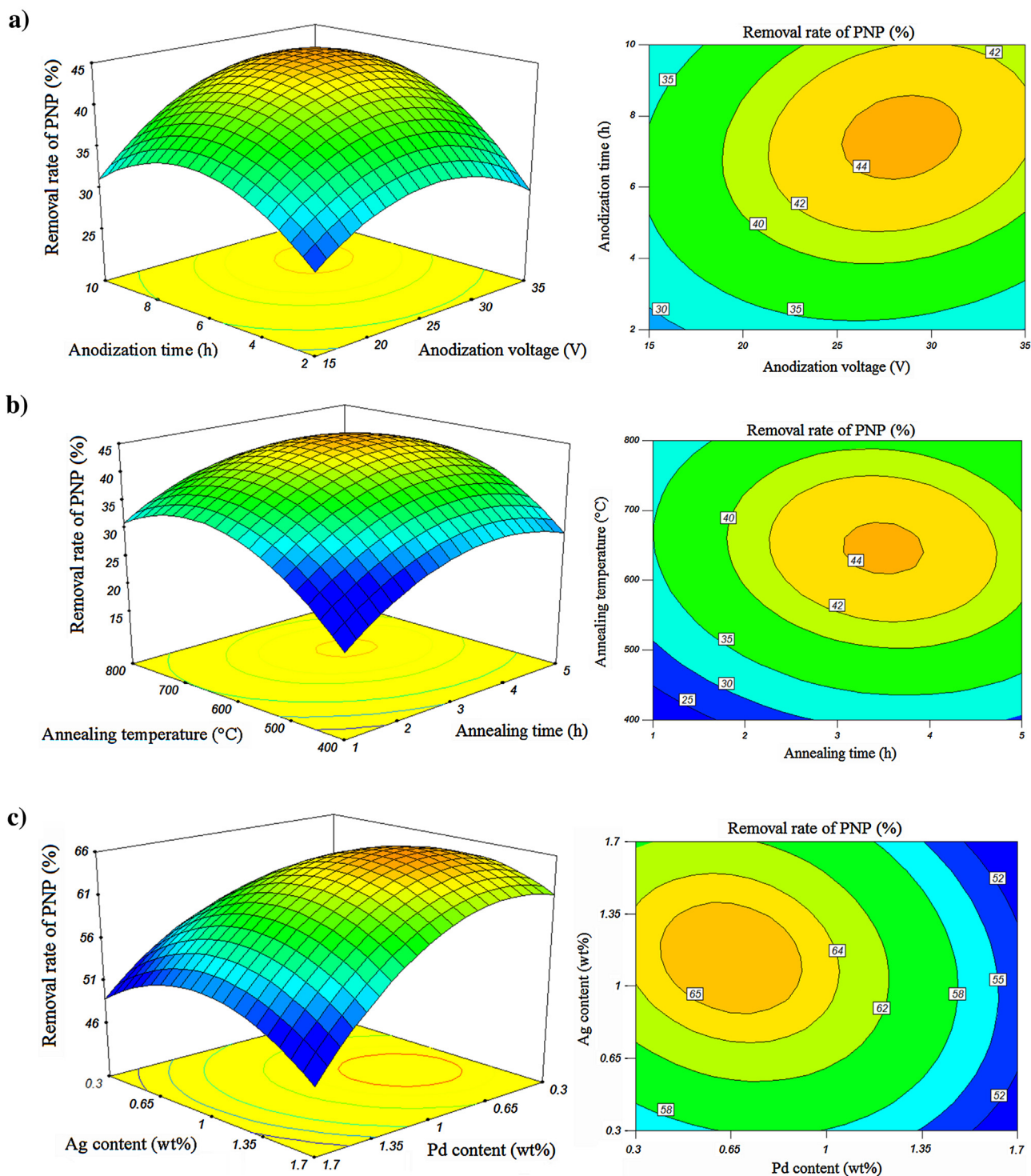


Fig. 2. The 3-D response surface and 2-D contour plots of photoelectrocatalytic removal of PNP (a and b) over TiO_2 -NTAs (as a function of anodization variables; (a) interaction between anodization voltage and anodization time (annealing temperature of 600°C and annealing time of 3 h), (b) interaction between annealing temperature and annealing time (anodization voltage of 25 V and anodization time of 6 h)), and (c) over Pd, Ag NPs/ TiO_2 -NTAs (as a function of metals content; interaction between Pd and Ag contents).

taining 0.2% H_2O) and 0.4 wt% NH_4F . Preliminary experiments were performed to determine a suitable concentration of NH_4F . The electrochemical cell consisted of a two-electrode configuration with graphite plate as cathode and titanium foil as anode ($3\text{ cm} \times 3\text{ cm}$). The distance between cathode and anode was 5 cm. Experiments were carried out at room temperature under vigorous stirring of the solution, at constant cell voltage in the range of 15–35 V. After

anodic oxidation, the obtained samples were thoroughly rinsed with deionized water, ultrasonically treated (ca. 100 W) in acetone for 30 min, dried with nitrogen gas flow, and finally the amorphous titania was crystallized by heat treatment in air at different temperatures in the range 400 – 800°C for 1–5 h. Fig. 1 shows the steps of the process and the photoelectrochemical reaction system with the proposed reaction mechanism.

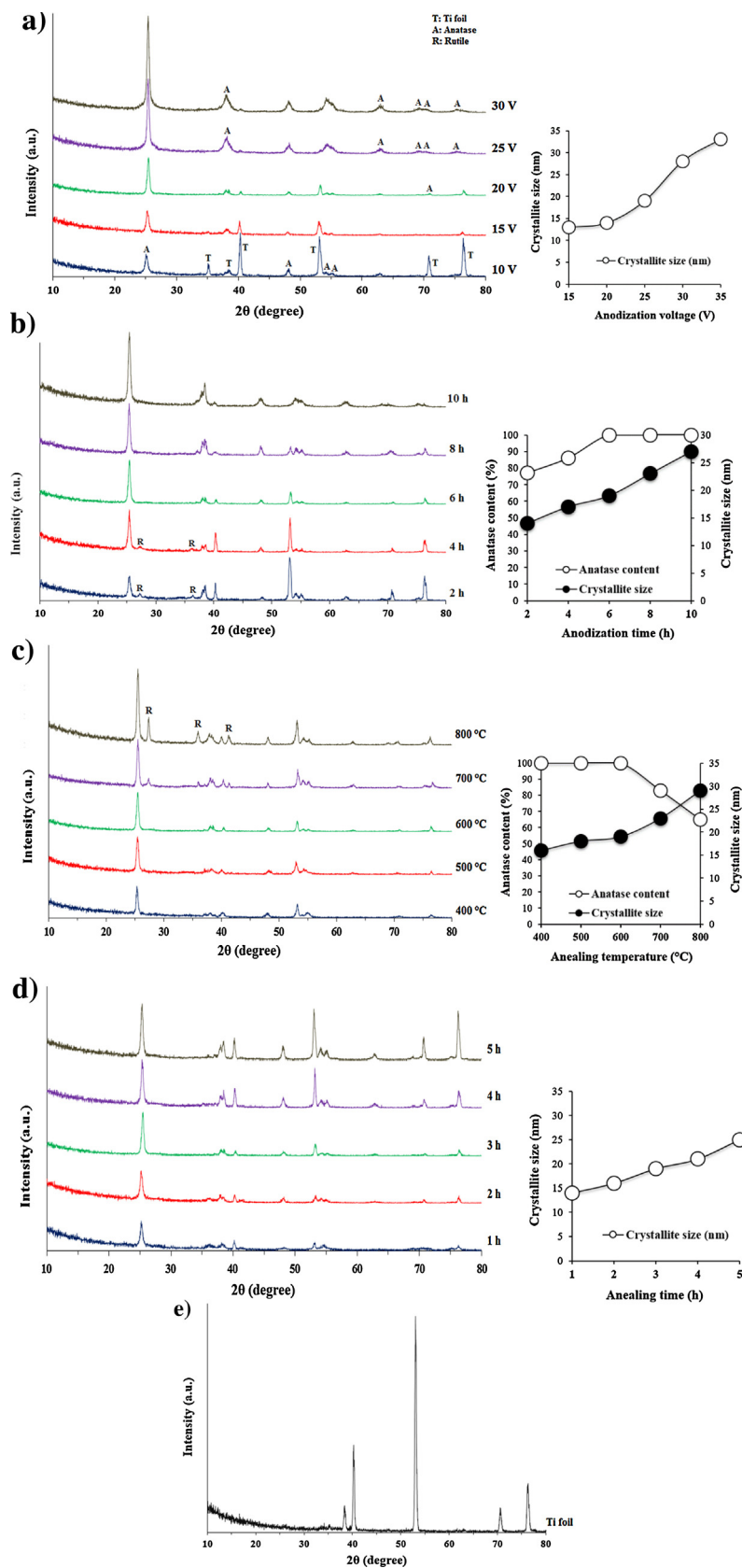


Fig. 3. XRD patterns of (a–d) TiO_2 -NTAs (as a function of (a) anodization voltage (anodization time of 6 h, annealing temperature of 600 °C, and annealing time of 3 h), (b) anodization time (anodization voltage of 20 V, annealing temperature of 600 °C, and annealing time of 3 h), (c) annealing temperature (anodization voltage of 20 V, anodization time of 6 h, and annealing time of 3 h), (d) annealing time (anodization voltage of 20 V, anodization time of 6 h, and annealing temperature of 600 °C,)) and (e) Ti substrate.

Table 1

Experimental ranges and levels of the tested variables.

Variables	Ranges and levels				
	−2	−1	0	+1	+2
Anodization and annealing variables					
Anodization voltage (V)	15	20	25	30	35
Anodization time (h)	2	4	6	8	10
Annealing temperature (°C)	400	500	600	700	800
Annealing time (h)	1	2	3	4	5
Metals content					
Pd content (wt%)	0.3	0.5	1	1.5	1.7
Ag content (wt%)	0.3	0.5	1	1.5	1.7

2.3. Preparation of anatase-type TiO₂-NTAs decorated with Pd, Ag clusters

Sodium borohydride was used as reducing chemical for the deposition of metallic Pd and Ag clusters on the surface of TiO₂-NTAs. Hydrides can effectively reduce Pd²⁺ and Ag⁺ ions to metallic species at room temperature [18,19]. For this purpose, the anatase-type TiO₂-NTAs plates were immersed in deionized water containing the required amounts of Pd²⁺ and Ag⁺ ions. Then the NaBH₄ solution (50 mg L^{−1}) was added drop-wise to the reaction mixture for 1 h under ultrasonication. Finally, the plates were dried with the nitrogen gas flow. The samples were named as Pd,Ag-NPs/TiO₂-NTAs for bimetallic clusters, and Pd-NPs/TiO₂-NTAs and Ag-NPs/TiO₂-NTAs for single metal clusters prepared under similar conditions as described for Pd,Ag-NPs/TiO₂-NTAs.

2.4. Characterization methods

Crystallographic analysis was carried out by X-ray diffraction (XRD) using Cu Kα radiation (λ = 0.15478 nm) (Philips generator PW 1830, goniometer PW 3020). The (1 0 1) reflection (2θ = 25.28°) of anatase and the (1 1 0) reflection (2θ = 27.42°) of rutile were used for analysis. The average TiO₂ crystallite size was calculated from the line broadening of corresponding reflections according to Scherrer's equation [20]

$$D = \frac{k\lambda}{\beta \cos \theta} \quad (1)$$

where *D* is the average crystallite size (nm), λ is the wavelength of the X-ray radiation, *k* is a constant taken as 0.89, β is the full width at half maximum intensity, and θ is the half diffraction angle.

The phase content in the samples was calculated by the following equation [21]

$$\text{Rutile phase\%} = \frac{100}{1 + 0.8 (I_A/I_R)} \quad (2)$$

where *I_A* is the integrated intensity of anatase (1 0 1) diffraction peak and *I_R* is the integrated intensity of rutile (1 1 0) diffraction peak.

The surface morphology and distribution of the nanotubes and nanoparticles were observed by using a scanning electron microscope (SEM, Zeiss EVO 50 EP) equipped with an energy dispersive spectrometer (EDS) system for analyzing the chemical composition of the samples. Particle size and distribution of the Pd and Ag nanoparticles were obtained by high-resolution transmission electron microscopic (HRTEM, Philips CM200 FEG, 200 kV) studies. The actual contents of Pd and Ag metals in the samples were also determined by X-ray fluorescence (XRF, Fischerscope XAN FD) and inductive coupled plasma atomic emission spectrometry (ICP-AES, Varian-Australian). For the ICP-AES measurement the samples were dissolved in HF and HNO₃ solutions. X-ray photoelectron spectroscopy (XPS) was used to study the chemical state of samples using a VG Microtech, twin anode XR3E2 X-ray

source. Photoluminescence emission spectra were recorded using a Varian Cary-Eclipse luminescence spectrometer (Agilent Technologies) with excitation wavelength at 320 nm. UV–vis DRS was obtained using AvaSpec-2048 TEC spectrometer for determination of the optical band-gap energy and calculated by the following equation [22];

$$E_g = \frac{hc}{\lambda} \quad (3)$$

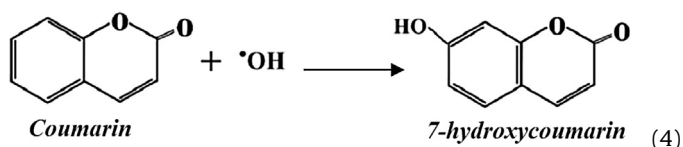
where *E_g* is the optical band-gap energy, *h* is the Planck's constant, *c* is the light speed, and λ is the wavelength.

2.5. Photoelectrocatalytic experiments

Photoelectrocatalytic degradation experiments were done at room temperature in a three-electrode configuration pyrex cell with graphite plate as counter electrode, the Pd,Ag-NPs/TiO₂-NTAs sample as anode, and a saturated calomel electrode (SCE, +0.24 V) as reference electrode. The counter electrode was held horizontally parallel to the working electrode at the distance of 5 cm. Artificial irradiation was provided by a 300 W halogen lamp (Osram), situated on top of the batch quartz reactor. The distance between the solution surface and the visible-light source was 10 cm. In each test, 100 mL of PNP solution (10 mg L^{−1}) and 0.05 M Na₂SO₄ as background electrolyte were transferred into the reactor and stirred for 30 min to achieve the adsorption equilibration in the dark before irradiation. The photoelectrocatalytic reaction was started by turning on the light source and applying a constant voltage of 0.6 V to the anode vs. SCE. At the given irradiation time, a sample (5 mL) was taken out from the solution, and PNP concentration measured by UV–vis spectrophotometry (λ_{max} = 317 nm).

2.6. Measuring of hydroxyl radicals

PL technique is a helpful method to detect the •OH radicals by measuring the fluorescence derived from the reaction of a non-or weakly-luminescent compound with •OH radicals and producing highly luminescent compound [23,24]. The formation rate of •OH radicals during visible-light irradiation of samples was detected by the PL technique using coumarin as a probe molecule. Coumarin readily reacted with •OH radicals to produce a highly luminescent product, 7-hydroxycoumarin (Eq. (4)) [25].



For this purpose, prepared plates and 20 mL of aqueous solution with 10^{−3} M of coumarin were transferred into the reactor, and stirred for 30 min (All conditions were the same as photoelectrocatalytic experiments). The high concentration of coumarin was utilized to capture all produced •OH radicals. After turning on

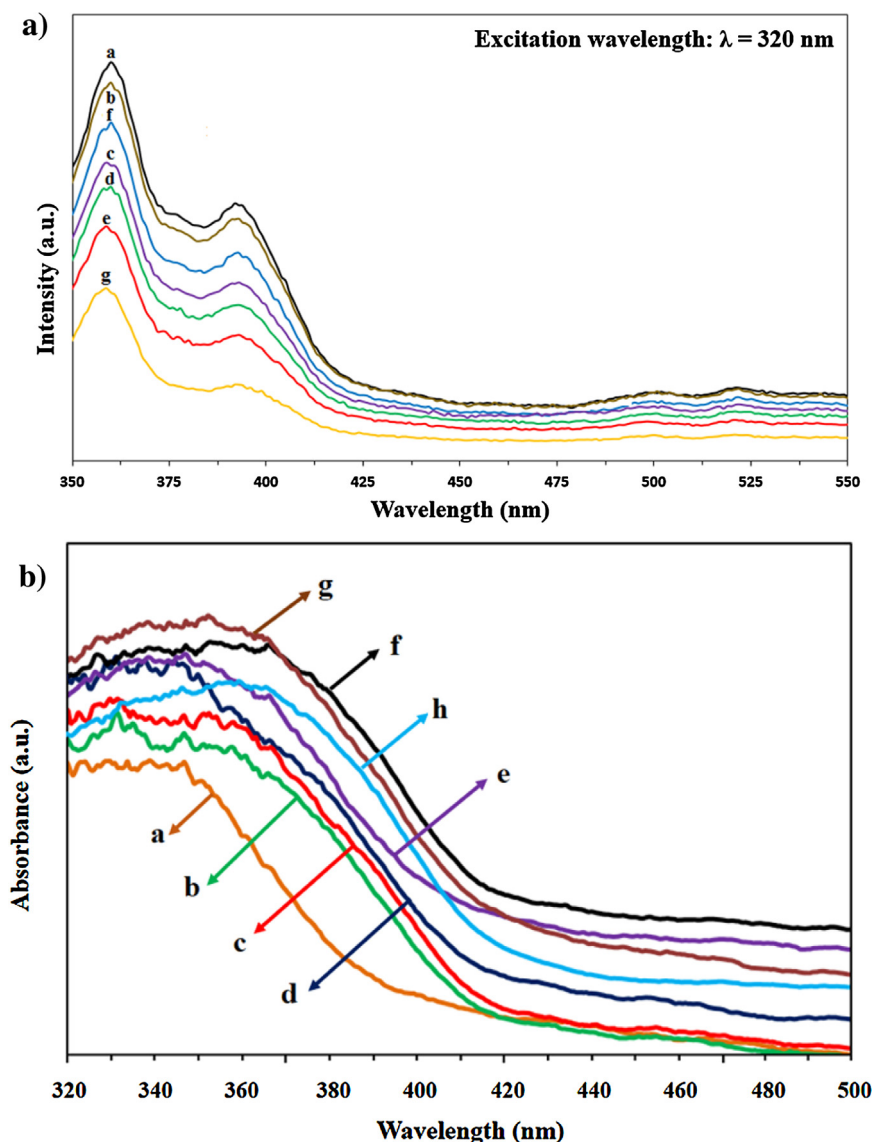


Fig. 4. (a) UV-vis DRS and (b) PL spectra of prepared samples (a) pure TiO_2 -NTAs, (b) $\text{Pd}(1 \text{ wt\%})$ -NPs/ TiO_2 -NTAs, (c) $\text{Ag}(1 \text{ wt\%})$ -NPs/ TiO_2 -NTAs, and (d–g) Pd,Ag -NPs/ TiO_2 -NTAs with different contents of deposited metals; ((d) $\text{Pd}(0.5 \text{ wt\%})$ - $\text{Ag}(0.5 \text{ wt\%})$), (e) $\text{Pd}(1 \text{ wt\%})$ - $\text{Ag}(1 \text{ wt\%})$, (f) $\text{Pd}(1.5 \text{ wt\%})$ - $\text{Ag}(1.5 \text{ wt\%})$, (g) $\text{Pd}(0.5 \text{ wt\%})$ - $\text{Ag}(1.5 \text{ wt\%})$, and (h) $\text{Pd}(1.5 \text{ wt\%})$ - $\text{Ag}(0.5 \text{ wt\%})$).

the light source, the samples were withdrawn from the reactor at given irradiation times, and then the PL emission spectra of the produced 7-hydroxycoumarin recorded using a PL spectrometer with excitation wavelength at 456 nm.

2.7. Experimental design

The response surface methodology based on central composite design (CCD) was used to define a mathematical model of the photoelectrocatalytic process. Computational analysis of the experimental data was supported by the Design-Expert (version 7) software. In order to evaluate the influence of effective variables, the following six key factors were selected, anodic oxidation voltage, anodic oxidation time, annealing temperature, annealing time, Pd and Ag contents, and the photoelectrocatalytic removal rate of PNP was chosen as the response. The experimental ranges and the levels of the variables are presented in Table 1. It should be noted that, preliminary experiments were performed to determine the extreme values of the variables.

3. Results and discussion

3.1. Optimization of anodization and annealing variables

The details of the experiments for anodization and annealing variables along with experimental results for the removal rate of PNP are presented in Table 2. Three-dimensional surface plots are the useful approach in revealing the effect of variables and the two-dimensional contour plots help in identification the interactions between variables. The 3D response surface and the 2D contour plots for process variables are obtained, by keeping two variables constant and varying the other variables within the experimental ranges. The 3D response surface and the 2D contour plots are shown in Fig. 2.

The XRD patterns of TiO_2 -NTAs are shown in Fig. 3. For comparison, the XRD pattern of the Ti substrate is also shown in Fig. 3(e). The reflections at 2θ of 25.4° , 38.1° , 48.1° , 54° , 55.2° , 62.7° , 69.1° , 70° , and 75.3° are attributed to anatase, reflections at 2θ of 27.5° , 37.9° , and 41.3° are attributed to rutile, and reflections at 2θ of 36.1° , 38.3° , 40.2° , 53.1° , 70.7° , and 76.1° are attributed to Ti substrate.

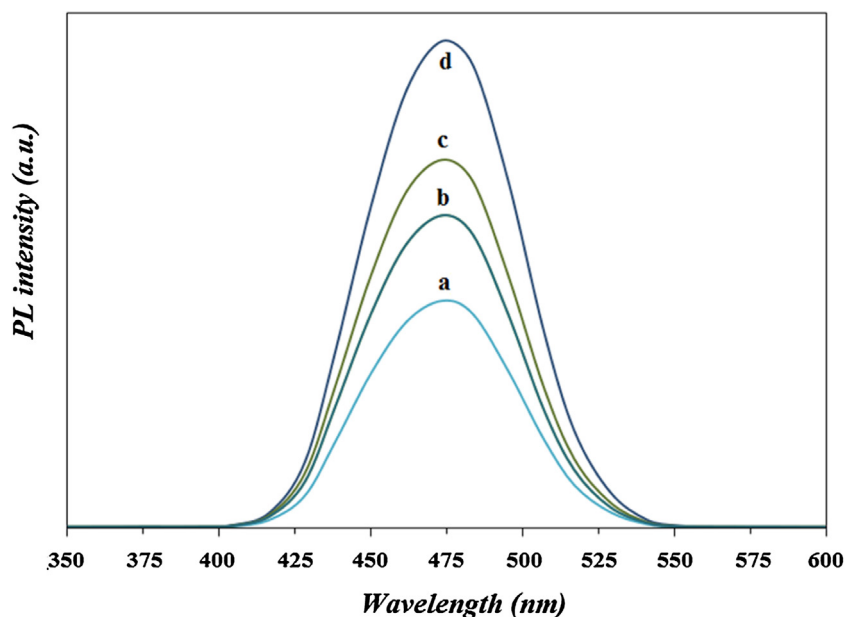


Fig. 5. PL spectral changes observed during visible-light irradiation of prepared samples in a 10^{-3} M of coumarin solution ((a) pure TiO_2 -NTAs, (b) Pd(1 wt%)-NPs/ TiO_2 -NTAs, (c) Ag(1 wt%)-NPs/ TiO_2 -NTAs, and (d) Pd(0.72 wt%), Ag(1.26 wt%)-NPs/ TiO_2 -NTAs).

Table 2

The 4-factor CCD matrix for anodization and annealing variables with the experimental results for the removal rate of PNP.

Run	Anodization voltage (V)	Anodization time (h)	Annealing temperature ($^{\circ}\text{C}$)	Annealing time (h)	Removal rate of PNP (%)
1	30	8	700	2	45.4
2	15	6	600	3	34.1
3	20	4	700	4	43
4	30	8	700	4	47.6
5	30	4	500	2	34
6	25	6	400	3	33.4
7	25	6	600	3	43.2
8	25	6	600	3	42.7
9	20	8	500	4	41.3
10	20	4	700	2	42.2
11	30	8	500	2	39.5
12	30	4	700	2	41.8
13	25	6	600	5	33.1
14	25	6	800	3	26.6
15	25	2	600	3	29.3
16	25	6	600	3	44.1
17	20	8	700	2	36.6
18	20	8	700	4	45
19	30	8	500	4	43.6
20	20	4	500	4	31.7
21	25	6	600	3	43.5
22	25	6	600	3	43.9
23	35	6	600	3	32.7
24	20	8	500	2	31
25	30	4	500	4	35.9
26	25	10	600	3	35.9
27	20	4	500	2	26.6
28	25	6	600	1	31.8
29	25	6	600	3	43.1
30	30	4	700	4	46.2

The average TiO_2 crystallite sizes of anatase and rutile phases in TiO_2 -NTAs were calculated by means of Eq. (1) using the reflections of anatase at 25.3° and of rutile at 27.5° , respectively. The results of XRD analysis are summarized in Table 3. The structural properties of TiO_2 -NTAs are strongly affected by the process variables and the crystalline phase of TiO_2 in all samples is mainly anatase.

3.1.1. Interaction between cell voltage and time in anodic oxidation

Fig. 2(a) shows the effects of the anodic oxidation voltage and time on the removal rate of PNP, when annealing temperature

and time are kept at constant at 600°C and 3 h, respectively. It was observed that the photoelectrocatalytic activity of TiO_2 -NTAs is affected by the cell voltage, so that the removal rate of PNP increased from 34.1% to about 43% with an increase of voltage from 15 to 25 V. Further increasing to 35 V leads to a decrease in removal rate of PNP to 32.7%. Cell voltage plays an important role as it affects the migration rate of fluoride ions in the electrolyte and in the oxide, and causes the increase of the oxidation and dissolution rates [26]. Based on XRD results, it could be concluded that structural properties of TiO_2 -NTAs are affected by the anodic oxidation voltage. By increasing the cell voltage, the

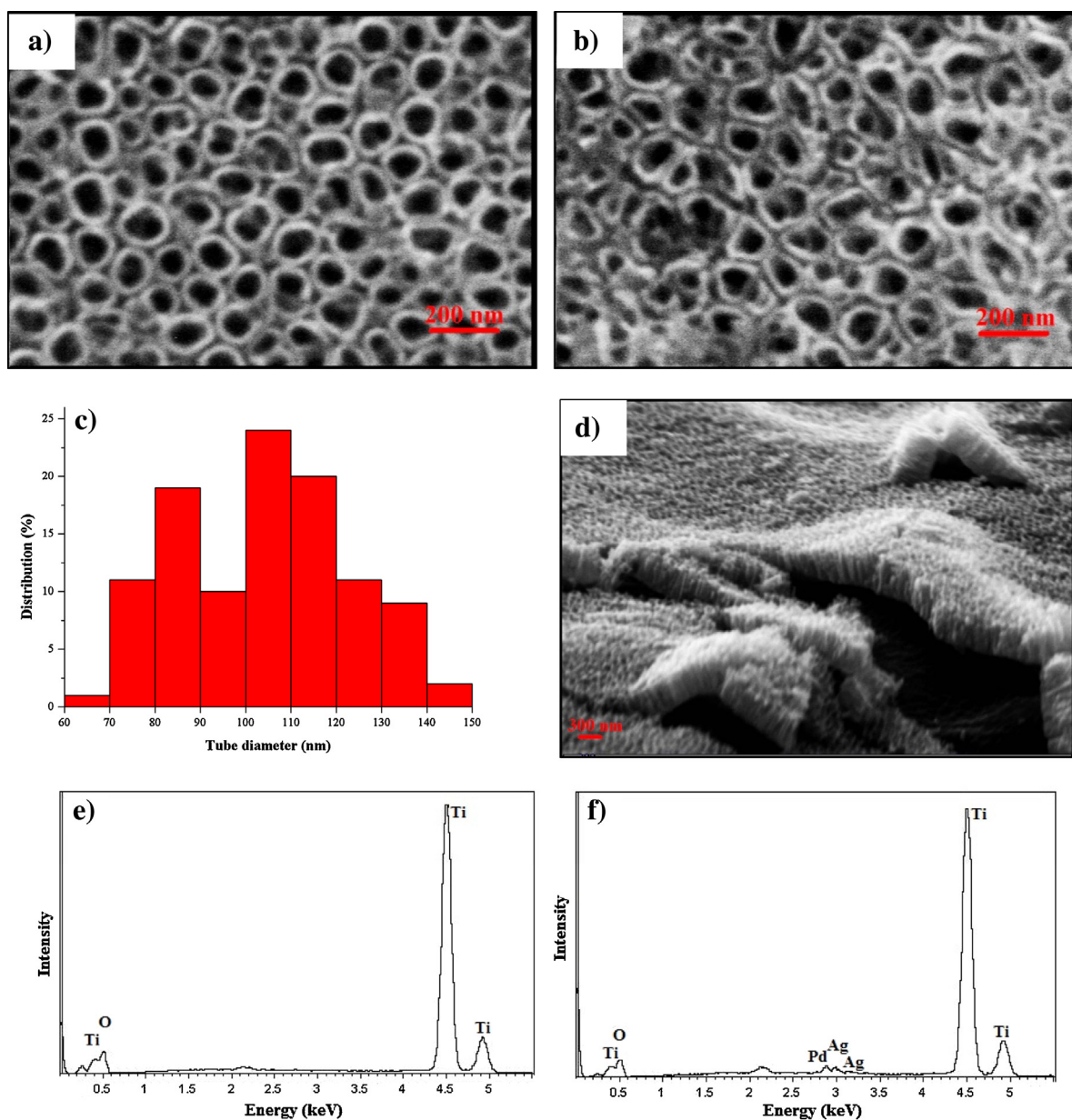


Fig. 6. (a and b) Top-view SEM micrographs ((a) TiO_2 -NTAs and (b) Pd,Ag-NPs/TiO_2 -NTAs), (c) distribution histogram of the nanotube mouth diameter, (d) cross-sectional SEM micrograph of TiO_2 -NTAs, and (e and f) EDS spectra ((e) TiO_2 -NTAs and (f) Pd,Ag-NPs/TiO_2 -NTAs), prepared under optimized conditions.

Table 3
Textural properties of TiO_2 -NTAs prepared under different anodization and annealing conditions.

Anodization voltage (V)	Anodization time (h)	Annealing temperature ($^{\circ}\text{C}$)	Annealing time (h)	Average crystallite size (nm)	Anatase phase (%)
15	6	600	3	13	100
20	6	600	3	14	100
25	6	600	3	19	100
30	6	600	3	28	100
35	6	600	3	33	100
25	2	600	3	14	77
25	4	600	3	17	86
25	8	600	3	23	100
25	10	600	3	27	100
25	6	400	3	16	100
25	6	500	3	18	100
25	6	700	3	23	83
25	6	800	3	29	65
25	6	600	1	14	100
25	6	600	2	16	100
25	6	600	4	21	100
25	6	600	5	25	100

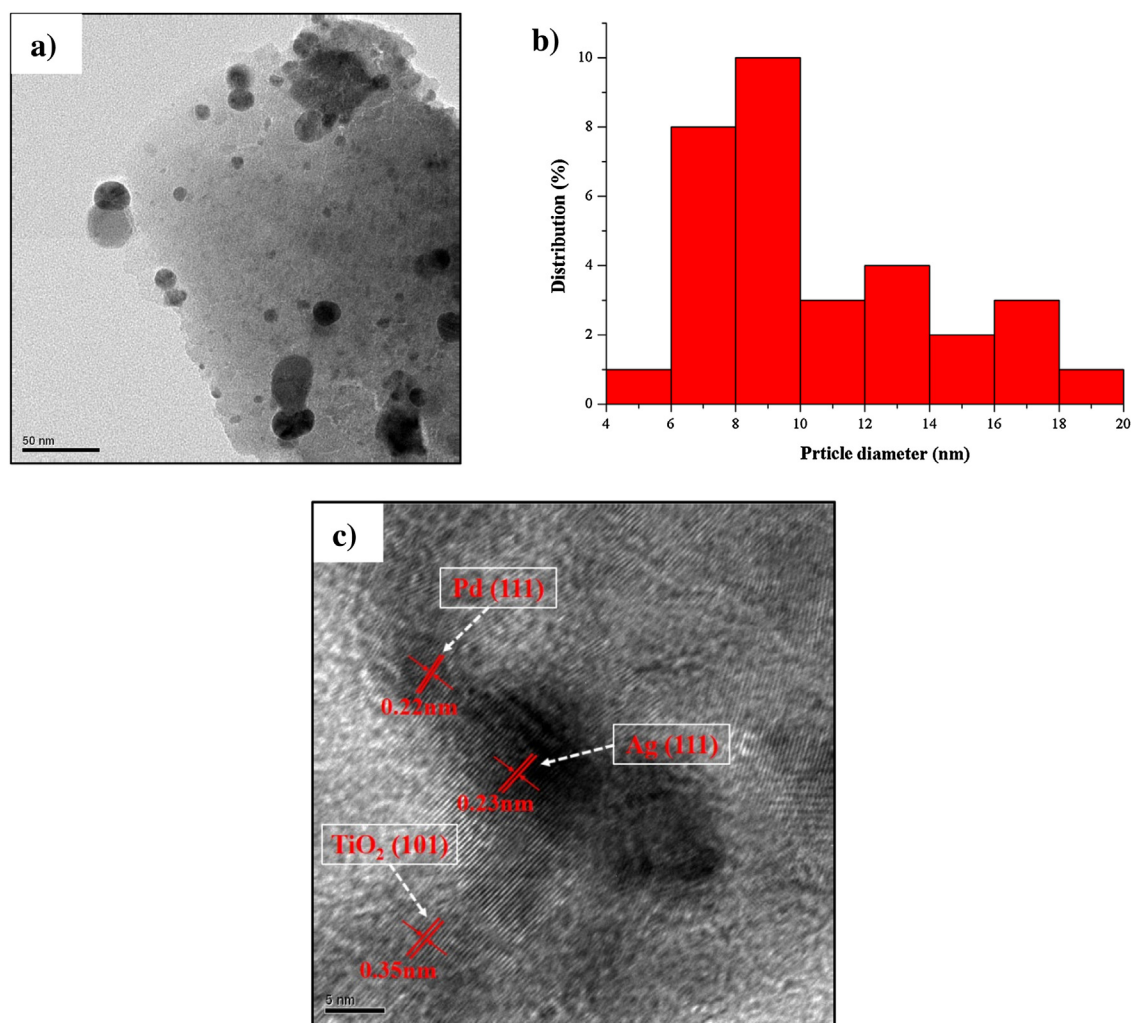


Fig. 7. (a) TEM image of the Pd,Ag-NPs/TiO₂-NTAs, (b) distribution histogram of the metal particles diameter, and (c) HRTEM image of the Pd,Ag-NPs/TiO₂-NTAs, prepared under optimized conditions.

intensities of anatase reflections grow while the intensities of substrate reflections become weaker, due to higher thickness of the nanotube layers obtained by increasing the anodization voltage. No anatase to rutile transformation was detected in thermally treated TiO₂-NTAs, whereas around 30 V is reported as the typical voltage value for structural transformation to rutile in TiO₂ nanotubes after thermal treatment [27]. The line broadening of anatase reflections decreases with the increase of the anodization voltage. The average TiO₂ crystallite size in the TiO₂-NTAs calculated from the Scherrer's equation increased from 13 to 33 with an increase in anodic oxidation voltage from 15 to 35. The same observation was reported by Alivov et al. [28], so that the intensity of (101) reflection of the anatase structure increased with increasing the voltage from 10 to 30 V and remained unchanged until 120 V. The high anodic oxidation voltages increase fluoride ion concentration at the tubes bottom and produce higher electric field strength in the electrolyte. The local temperature rise due to the enhanced joule heating and the higher field strength across the oxide layer will both accelerate the crystallization of the oxides grown [29]. In the field of photocatalytic applications, it is generally accepted that the anatase phase of TiO₂ has higher activity in comparison with other phases, which can be attributed also to the ability of anatase phase in generation of more mobile •OH radicals [30,31]. As well as, the photocatalytic activity of TiO₂ also depends on the crystallite size. It has been commonly accepted that small crystallite size decreases the recom-

bination chances of photoinduced electron-hole pairs due to of their faster arrival at the reaction site on the TiO₂-NTAs surface [32]. However, when the crystallite size is smaller than a certain limit, most of the photoinduced electron-hole pairs are generated very near to the surface of the catalyst that in this case the surface recombination electron-hole pairs occurs faster than interfacial transfer process [33,34]. Therefore, there is an optimal crystallite size for the TiO₂ catalyst to obtain the high photocatalytic activity. TiO₂-NTAs sample anodized at 25 V and thermally treated at 600 °C for 3 h, have pure anatase phase with 19 nm crystallite size gives higher photoelectrocatalytic activity than the other samples.

Besides, it was observed that the duration of anodic oxidation affects the photoelectrocatalytic activity of TiO₂-NTAs, as demonstrated by experiments conducted with different times in the range from 2 to 10 h. As it can be seen from Fig. 2(a) and Table 2, an increase in the anodic oxidation time from 2 to 6 h increases the removal rate of PNP from 29.3% to 43%. Based on XRD results, it could be concluded that by increasing the anodic oxidation time, the intensity of the substrate and rutile phase reflections of the thermally treated samples decreased while the intensity of anatase reflections gradually increased and the anatase appears to be the major phase of TiO₂-NTAs, which can be caused by larger thickness of the TiO₂-NTAs layers. Longer anodization times are related to a decrease of the rutile content in the thermally treated samples, so that after 4 h of anodic oxidation, a 86:14 anatase-rutile

mixture was obtained. The rutile phase completely disappeared in TiO₂-NTAs sample prepared by anodic oxidation of 6 h, and only anatase was obtained. The dependence of TiO₂ crystal structure on anodic oxidation time can be ascribed in the thermally treated samples to the initial nucleation of the rutile layer at the interface between the Ti substrate and TiO₂, followed by the formation of near pure anatase phase [35]. Altomare et al. [35] studied the effect of anodic oxidation duration on structural properties of TiO₂ nanotubes annealed for 3 h at 450 °C. They have found a 60:40 anatase:rutile mixture for TiO₂ nanotubes obtained after 20 min of anodic oxidation, while longer experiments led to an increase of the anatase content and after 7 h of anodic oxidation a nearly pure anatase structure was obtained. Furthermore, the average crystallite size of anatase phase slightly increased from 14 to 27 nm by prolonging the anodization time. The smallest crystallite size (14 nm) was achieved for anatase phase in the TiO₂-NTAs prepared by anodic oxidation time of 2 h. In any case, TiO₂-NTAs sample anodized for 6 h, having pure anatase phase and crystallite size of 19 nm gives higher photocatalytic activity than the other samples. The contour plots (Fig. 2(a)) show that the optimum region for highest removal rate of PNP ($\geq 44\%$) is achieved by performing anodic oxidation in the range 26–31 V for 6.5–8.5 h, when the annealing temperature and time are kept at constant 600 °C and 3 h, respectively.

3.1.2. Interaction between annealing temperature and annealing time

In order to find out the effect of annealing temperature on photoelectrocatalytic activity of TiO₂-NTAs, the samples were annealed at temperatures between 400 and 800 °C. Fig. 2(b) shows the effect of the annealing temperature and time on the removal rate of PNP, when anodic oxidation voltage and time are kept at constant 25 V and 6 h, respectively. As can be seen, the removal rate of PNP increased from 33.4% to about 43% with increasing the annealing temperature from 400 to 600 °C. It is well known that the annealing temperature is the key parameter which influences the phase structure of TiO₂. XRD results reveal that the TiO₂-NTAs annealed between 400 and 600 °C exist solely as anatase phase. No structural transformation from anatase to rutile was detected after annealing at 600 °C, whereas the typical temperature that generally is expected for anatase–rutile transition was reported to be around 430–600 °C [36–40]. XRD results reveal that calcined samples at 700–800 °C are a combination of anatase and rutile phases of TiO₂. The report by Varghese et al. [39] found that the anatase to rutile transition started at 430 °C and ended in pure rutile at 620 °C. Li et al. [40] found only the anatase structure after annealing at between 300 and 500 °C, while the rutile structure started to appear at 600 °C. Refs. [28,38,41,42] reported temperature of 800 °C for complete transformation into rutile structure. However, much lower stability for TiO₂ nanotubes was reported by Jaroenworarluck et al. and Regonini et al. [43,44]. They found that the rutile structure appeared at 500 °C and became dominant at 600 °C. The reported annealing temperatures for anatase–rutile transition are much lower than those obtained in this study. TiO₂-NTAs produced in acetic acid have a quite stable anatase structure, so that with increasing annealing temperature to 800 °C, only some portion of anatase phase transformed into rutile phase. Acetic acid plays a significant role in stabilizing the anatase structure of TiO₂, as has been reported by several groups [11,45,46]. Schlott et al. [46] reported that the anatase fraction in TiO₂ nanotubes can be increased by using a diethylene triamine penta acetic acid in the electrolyte composition. The improved thermal stability is useful to improve the photocatalytic activity, because the higher level of TiO₂ crystallinity can be obtained by annealing at high temperatures without forming the rutile structure which is responsible for the low photocatalytic activity of TiO₂. Generally, an appropriate annealing temperature

is required for preparation of the desired structure of TiO₂-NTAs with highest photoelectrocatalytic activity. Results show that the photoelectrocatalytic activity decreased if annealing temperature became higher than about 710 °C. In fact, it can be attributed to the growth of crystallite size, reduction of adsorbed water molecules, and appearance of the rutile phase [47]. High annealing temperature enhances the atomic mobility and causes grain growth [48]. The same results were also reported in Refs. [41,42]. The highest removal rate of PNP was obtained by TiO₂-NTAs annealed at 600 °C with pure anatase structure and crystallite size of 19 nm.

In order to find out the effect of annealing time on the photoelectrocatalytic activity of TiO₂-NTAs, the samples were annealed for different durations of time (1–5 h). It can be seen from Fig. 2(b) that the increase in the annealing time from 1 to 3 h improves the removal rate of PNP from 31.8% to about 43%. XRD results reveal that the crystallinity of the anatase structure improved with increasing annealing time. The crystallinity of TiO₂ is a key factor affecting the photocatalytic activity, so that the anatase structure with a high crystallinity degree has less bulk defects which act as a recombination centers for photoinduced electron–hole pairs [49]. The same result was reported by Nischk et al. [16], crystallinity of the anatase structure increased with increasing annealing time from 1 to 6 h at 450 °C. The higher photoelectrocatalytic activity of the TiO₂-NTAs annealed for 3 h is consistent with an improved crystallinity degree of its anatase structure. Nevertheless, prolonging the annealing time at a fixed temperature was not beneficial for the photoelectrocatalytic activity and resulted in larger crystallite size. As it can be seen from results in Table 3, if the annealing time passes from 3 to 5 h, the crystallite size of anatase structure was increased from 19 nm to 25 nm. The highest removal rate of PNP was obtained by TiO₂-NTAs annealed for 3 h with a pure anatase structure and crystallite size of 19 nm. The contour plots (Fig. 2(b)) show that the optimum region for highest removal rate of PNP ($\geq 44\%$) is achieved using annealing temperature in the range 610–710 °C and annealing time higher in the range 3–4 h, when the anodization temperature and time are kept at constant 25 V and 6 h, respectively. The photoelectrocatalytic removal rate of PNP was defined by the optimum values of anodic oxidation variables in the selected range using Design Expert as a response optimizer software. The optimal values of the anodic oxidation variables for the maximum removal rate of PNP (53.5%) are 27.4 V, 441 min, 642 °C, and 207 min for anodic oxidation voltage and time, and annealing temperature and time, respectively.

3.2. Optimization of Pd and Ag contents

In the next stage, anatase-type TiO₂-NTAs prepared under optimized anodic oxidation and thermal treatment conditions was chosen, and the effect of Pd and Ag deposition on its efficiency was optimized using RSM technique. The details of the experiments along with experimental results for the removal rate of PNP are presented in Table 4.

3.2.1. Interaction between Pd and Ag contents

The 3D response surface and the 2D contour plots (Fig. 2(c)) for Pd and Ag contents are obtained by using the statistical software to evaluate the interactive relationships between the metals content and the removal rate of PNP. The results showed that the photoelectrocatalytic activity of TiO₂-NTAs increased with the increase of Pd and Ag contents up to 1 wt%. As it can be seen from Table 4, the removal rate of PNP increased from 61.6% and 58.6% to about 64.1% by increasing the Pd and Ag contents from 0.3 to 1 wt%, respectively.

The positive effect of Pd and Ag nanoparticles is associated with their scavenging ability of the electrons promoted in the conduction band of TiO₂-NTAs [50–55]. The metal nanoparticles onto the TiO₂-NTAs surface can act as effective electron traps by the indirect

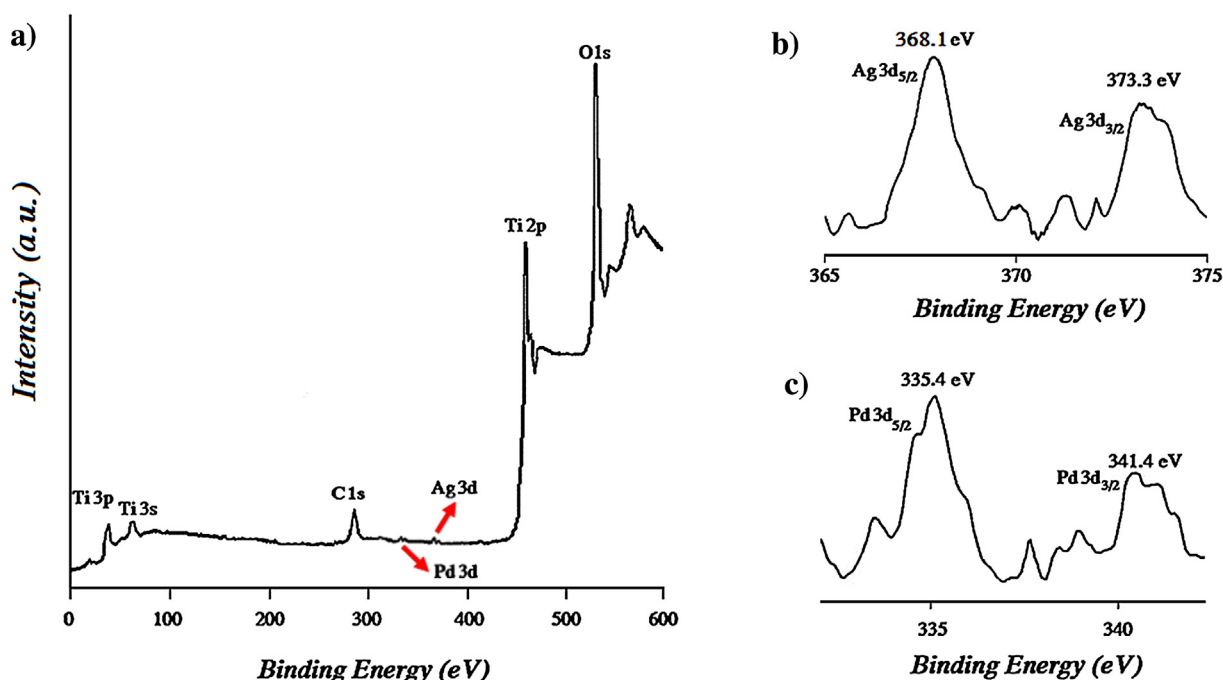


Fig. 8. XPS spectra of Pd,Ag-NPs/TiO₂-NTAs prepared under optimized conditions: (a) a wide survey scan and (b and c) the magnified regions ((b) Ag 3d and (c) Pd 3d).

Table 4

The 2-factor CCD matrix for Pd and Ag contents with the experimental results for the removal rate of PNP.

Run	Pd content (wt%)	Ag content (wt%)	Removal rate of PNP (%)
1	1	1	64.1
2	0.5	0.5	61.2
3	1	1.7	56.4
4	0.3	1	61.6
5	1.5	0.5	54.3
6	1	1	63.9
7	0.5	1.5	67.9
8	1	0.3	58.6
9	1	1	64.5
10	1	1	64.9
11	1.5	1.5	57.1
12	1	1	64.3
13	1.7	1	52.7

modification of the interfacial charge transfer mechanism. Metal nanoparticles in contact with the surfaces of TiO₂-NTAs form Schottky barriers. Since the Fermi level of noble metals is lower than the conduction band of TiO₂, charge carriers will transfer from the conduction band of TiO₂ to metal nanoparticles. In fact, the Schottky barrier can trap photoinduced electrons, and thus effectively inhibits the recombination rate of photoinduced electrons–holes pairs [4–7]. The electrons transferred to the surface of TiO₂-NTAs react with adsorbed O₂ molecules to form O₂^{•−} ions [56]. On the other hand, more photoinduced holes can diffuse to the TiO₂-NTAs surface and oxidize the adsorbed H₂O molecules or OH[−] ions to create •OH radicals (Eqs. (5) and (6)) [57]. In the photocatalytic processes hydroxyl radicals as very powerful oxidizing agents are responsible for degradation of organic compounds as well as by-products [58].



Moreover, noble metal nanoparticles have plasmon resonance in the optical range of UV and near-UV–vis light, which promotes photon absorption. Noble metal nanoparticles can harvest and

transfer more light energy to the TiO₂-NTAs at the energies both above and below the band edge by resonant energy transfer [59,60]. Thus the presence of Pd and Ag nanoparticles leads to the generation of more electron–hole pairs under light irradiation, which helps to improve the photoelectrocatalytic activity.

An excessive content of Pd and Ag metals give a negative effect on the photoelectrocatalytic activity of the TiO₂-NTAs. This negative behavior can be attributed to increasing the size and number of metal nanoparticles onto TiO₂-NTAs that act as recombination centers for photoinduced electron–hole pairs. Also, more numbers of metal nanoparticles can decrease the accessibility of the active sites and shadow the surface of TiO₂-NTAs from visible-light absorption [61–63]. Therefore, there was an appropriate content of metals for the most efficient separation of photoinduced electron–hole pairs. The Pd and Ag contents in samples were determined by XRF and ICP-AES analysis and the results are shown in Table 5. It can be seen that the actual contents of Pd and Ag metals are very close to the predetermined values in all cases.

To study the recombination of electrons–holes pairs, the PL spectrum of the TiO₂-NTAs with different contents of Pd and Ag was measured. The PL emission in oxide semiconductors arises from the recombination of free charge carriers [64,65]. Fig. 4(a) shows the PL spectra of the single and bimetallic particles deposited TiO₂-NTAs excited with a source emitting at 320 nm. A significant decrease in PL intensity of TiO₂-NTAs with an increase in Pd and Ag contents was observed. The weaker PL intensity suggests that Pd and Ag nanoparticles onto the TiO₂-NTAs surface could effectively limit the recombination of photoinduced electron–hole pairs. However, a significant decrease in the PL intensity was observed for Pd(0.5 wt%)-Ag(1.5 wt%)/TiO₂-NTAs sample. In fact, simultaneous deposition of Pd and Ag with optimal content leads to a synergistic effect in the scavenging of photoinduced electrons and results in further enhancement of photoelectrocatalytic activity.

DRS spectra were carried out to assess the optical property of TiO₂-NTAs (Fig. 4(b)). The absorption wavelengths for TiO₂-NTAs deposited with Pd and Ag nanoparticles were significantly red shifted. The absorption of Pd and Ag simultaneously deposited TiO₂-NTAs in the visible-light region is more than the pure and

Table 5
Different characteristics of pure and Pd, Ag deposited TiO₂-NTAs samples.

Sample	Metals contents (wt%)		Absorption thresholds (nm)	Eg (eV)	Actual metals contents (wt%)			
	Pd	Ag			XRF		ICP-AES	
					Pd	Ag	Pd	Ag
TiO ₂ -NTAs	–	–	398	3.11	–	–	–	–
Pd-NPs/TiO ₂ -NTAs	1	–	418	2.96	0.97	–	0.94	–
Ag-NPs/TiO ₂ -NTAs	–	1	422	2.94	–	0.98	–	0.91
Pd,Ag-NPs/TiO ₂ -NTAs	0.5	0.5	427	2.9	0.47	0.46	0.42	0.44
Pd,Ag-NPs/TiO ₂ -NTAs	1	1	430	2.88	0.96	0.97	0.91	0.92
Pd,Ag-NPs/TiO ₂ -NTAs	1.5	0.5	433	2.86	1.45	0.48	1.43	0.4
Pd,Ag-NPs/TiO ₂ -NTAs	0.5	1.5	438	2.83	0.46	1.44	0.45	1.39
Pd,Ag-NPs/TiO ₂ -NTAs	1.5	1.5	442	2.80	1.48	1.47	1.44	1.45

mono-deposited ones that suggest higher photocatalytic activity for Pd,Ag-NPs/TiO₂-NTAs sample under visible-light irradiation. The absorption thresholds and E_g values calculated from the Eq. (3) are reported in Table 5. Results indicate that Pd and Ag deposition onto TiO₂-NTAs decreased optical band-gap energy, whereas a decrease in E_g value for simultaneously deposited samples is higher than for mono-deposited. The electron transition from the valence band to the conduction band occurs easier with band-gap narrowing in semiconductors [66]. However, it should be noted that when the band-gap in oxide semiconductors becomes very narrow the recombination of the photoinduced charge carriers occurs easier [67]. It can be concluded that an optimal band-gap width is required for high photocatalytic efficiency.

The contour plots (Fig. 2(c)) shows that the optimum region for highest removal rate of PNP ($\geq 61\%$) is achieved using Pd and Ag contents in the range of about 0.4–0.85 and 0.9–1.35, respectively.

The main objective in term of photoelectrocatalytic activity is related to optimum values of Pd and Ag contents calculated by using Design Expert as a response optimizer software. The optimal values of the Pd and Ag contents for the maximum removal rate of PNP (72.7%) are achieved 0.72 and 1.26 wt%, respectively. Whereas, the removal rate of PNP in the presence of pure TiO₂-NTAs, Pd(1 wt%)-NPs/TiO₂-NTAs, and Ag(1 wt%)-NPs/TiO₂-NTAs samples was 53.5%, 56.9%, and 59.3%, respectively.

3.3. Formation of hydroxyl radicals

The coumarin fluorescence probe method was employed for detection the formation rate of •OH radicals during visible-light irradiation of pure TiO₂-NTAs, Pd(1 wt%)-NPs/TiO₂-NTAs, Ag(1 wt%)-NPs/TiO₂-NTAs, and Pd(0.72 wt%), Ag(1.26 wt%)-NPs/TiO₂-NTAs samples. Fig. 5 demonstrates the changes of the PL spectra for coumarin solution. For pure TiO₂-NTAs a weak PL signal was observed that indicates a low formation rate of •OH radicals (or 7-hydroxycoumarin) during visible-light irradiation. On the contrary, for Pd,Ag-NPs/TiO₂-NTAs, an intense signal of 7-hydroxycoumarin was observed that implies a high formation rate of •OH radicals (or 7-hydroxycoumarin) during visible-light irradiation.

3.4. SEM/EDS and HRTEM results

Fig. 6(a) and (b) show typical SEM micrographs of top-view of anatase-type TiO₂-NTAs before and after deposition with the Pd and Ag nanoparticles, respectively. They reveal the presence of TiO₂ nanotube arrays on Ti foil substrate grown by the anodic oxidation in CH₃COOH/NH₄F electrolyte. By comparing Fig. 6(a) and (b), it can be seen that the Pd and Ag nanoparticles are deposited on top of the nanotubes. Additionally, the tube-pore mouths are still open after the deposition, showing that pore structure can be maintained, which is very important for photocatalytic performance. Fig. 6(c)

shows a distribution histogram of the nanotube mouth diameter. The mean diameter of TiO₂ nanotubes mouth was approximately 100–110 nm. Fig. 6(d) shows an SEM micrograph of cross-section of anatase-type TiO₂-NTAs. These results indicate that the TiO₂-NTAs were about 500 nm in length. The chemical composition of the TiO₂-NTAs and Pd,Ag-NPs/TiO₂-NTAs was investigated with EDS analysis at the microscopic level. The results from EDS measurements (Fig. 6(e) and (f)) clearly confirmed the existence of Pd and Ag on the TiO₂-NTAs. Also, from EDS measurements the molar ratio of O:Ti was estimated to be 1.96:1, which is very close to the stoichiometry of TiO₂. It should be mentioned that the EDS results show the chemical composition of only the top surface of the TiO₂ nanotubes. From the TEM image (Fig. 7(a)), it is clear that the Pd and Ag nanoparticles were non-uniform deposited on the surface of TiO₂-NTAs. Fig. 7(b) shows a distribution histogram of the metal particles diameter. The mean diameter of Pd and Ag particles was approximately 8–10 nm. HRTEM image (7(c)) shows a single Ag, Pd nanoparticle deposited onto a TiO₂ nanotube. It shows three different lattice planes with spacing of 0.35, 0.23, and 0.22 nm. These three planes corresponded to the (1 0 1) plane of anatase TiO₂, the (1 1 1) plane of metallic Ag, and the (1 1 1) plane of metallic Pd, respectively.

3.5. XPS results

The surface composition and chemical states can be determined by means of XPS spectrum according to the characterizing binding energies of different elements on material surfaces [68]. The presence of metallic Pd and Ag on the surface of TiO₂-NTAs was confirmed by the XPS technique. The XPS spectrum of the Pd,Ag-NPs/TiO₂-NTAs is presented in Fig. 8(a) and the high-resolution XPS spectra of the binding energies for Ag 3d and Pd 3d are presented in Fig. 8(b) and (c), respectively. The low intensity of the Pd and Ag XPS peaks can be due to the low level of noble metals on the surface of TiO₂-NTAs [69,70]. The XPS peaks of Ag 3d located at around 368.1 and 373.3 eV, agreeing with the binding energy of Ag 3d_{5/2} and Ag 3d_{3/2}, respectively. The XPS peaks of Pd 3d located at around 335.4 and 341.4 eV, agreeing with the binding energy of Pd 3d_{5/2} and Pd 3d_{3/2}, respectively [70–73]. These results demonstrate that the Ag and Pd species on the surface of TiO₂-NTAs are mainly in metallic form. According to the binding energy handbook of the XPS apparatus, the binding energy of Ag⁺ and Ag⁰ is about 367.8 and 368.1 eV, respectively, while the binding energy of Pd²⁺ and Pd⁰ is about 336.4 and 335.3 eV, respectively. Therefore, the zero-valence noble metal atoms can be easily deposited on the TiO₂-NTAs surface via a chemical-reduction method. The presence of TiO₂ was also determined by the XPS analysis. The XPS peak located at around 458.5 eV is assigned to Ti 2p_{3/2} and another one located at around 464 eV corresponding to the Ti 2p_{1/2}, which are attributed to Ti⁴⁺ [74,75].

3.6. Reusability

The reusability of the catalysts is an important parameter and makes them effective for practical applications. Thus the reusability of Pd,Ag-NPs/TiO₂-NTAs prepared under optimized conditions was evaluated in the photoelectrocatalytic removal of PNP. In each run, the plate was recycled and then washed with deionized water several times. After drying in nitrogen gas flow, the Pd,Ag-NPs/TiO₂-NTAs was reused in the photoelectrocatalytic removal of fresh PNP solution. The results showed that after five times reuse cycle the removal rate of PNP had lost about 7%. These results clearly demonstrate that Pd,Ag-NPs/TiO₂-NTAs has high stability and reusability without decrease in photocatalytic performance.

4. Conclusions

Anatase-type Pd,Ag-NPs/TiO₂-NTAs as a new photocatalyst with enhanced catalytic efficiency were prepared by electrochemical anodic oxidation in CH₃COOH/NH₄F and thermal treatment, followed by a chemical-reduction method for Pd, and Ag cluster deposition. The stability of the anatase structure of TiO₂-NTAs in respect to varying anodic oxidation conditions was assessed by XRD results. A non-uniform distribution of Pd, Ag nanoparticles with an average particle size of 8–10 nm on the surface of TiO₂-NTAs (~500 nm length and ~100–110 nm diameter) was observed. DRS results showed a considerable decrease in band-gap energy value for co-deposited Pd, Ag particles onto TiO₂-NTAs in comparison with pure and single metallic species deposited onto TiO₂-NTAs. Compared with pure TiO₂-NTAs and Pd and Ag single metal clusters onto TiO₂-NTAs, the bimetallic clusters onto TiO₂-NTAs showed enhanced photoelectrocatalytic activity toward removal of PNP under visible-light irradiation. The enhanced activity was attributed to the electron scavenging ability of metal nanoparticles. From PL studies a considerable quenching with increasing the Pd and Ag contents in TiO₂-NTAs was observed that suggest the noble metals deposition could effectively inhibit the recombination probability of photoinduced electron-hole pairs. Finally, the effects of process parameters and Pd, Ag contents on the photoelectrocatalytic activity of TiO₂-NTAs were optimized using RSM technique. The results suggests that the relation between the phase structure and the photoelectrocatalytic activity is significant in the TiO₂-NTAs, and the crystallite structure of the TiO₂-NTAs can be controlled by anodic oxidation and thermal treatment parameters.

Acknowledgement

The authors would like to thank Politecnico di Milano for financial support of this work.

References

- [1] H. Eskandarloo, A. Badiei, M.A. Behnajady, *Ind. Eng. Chem. Res.* 53 (2014) 6881–6895.
- [2] A. Fujishima, K. Honda, *Nature* 238 (1972) 37–38.
- [3] H. Eskandarloo, A. Badiei, A.R. Tavakoli, M.A. Behnajady, G.M. Ziarani, *J. Mater. Educ.* 36 (2014) 111–116.
- [4] H. Eskandarloo, A. Badiei, M.A. Behnajady, G.M. Ziarani, *RSC Adv.* 4 (2014) 28587–28596.
- [5] M.A. Behnajady, H. Eskandarloo, *Chem. Eng. J.* 228 (2013) 1207–1213.
- [6] M.K. Seery, R. George, P. Floris, S.C. Pillai, *J. Photochem. Photobiol. A Chem.* 189 (2007) 258–263.
- [7] H. Eskandarloo, A. Badiei, M.A. Behnajady, G.M. Ziarani, *Chem. Eng. J.* 270 (2015) 158–167.
- [8] Y. Qu, X. Duan, *Chem. Soc. Rev.* 42 (2013) 2568–2580.
- [9] J. Li, S.K. Cushing, J. Bright, F. Meng, T.R. Senty, P. Zheng, A.D. Bristow, N. Wu, *ACS Catal.* 3 (2012) 47–51.
- [10] M. Pelaez, N.T. Nolan, S.C. Pillai, M.K. Seery, P. Falaras, A.G. Kontos, M.H. Entezari, D.D. Dionysiou, *Appl. Catal. B-Environ.* 125 (2012) 331–349.
- [11] M.A. Behnajady, H. Eskandarloo, N. Modirshahla, M. Shokri, *Photochem. Photobiol.* 87 (2011) 1002–1008.
- [12] Y.R. Smith, B. Sarma, S.K. Mohanty, M. Misra, *ACS Appl. Mater. Interfaces* 4 (2012) 5883–5890.
- [13] D. Guan, Y. Wang, *Nanoscale* 4 (2012) 2968–2977.
- [14] K.Y. Jung, S.B. Park, *Mater. Lett.* 58 (2004) 2897–2900.
- [15] Y.C. Chou, Y. Ku, *J. Chem. Eng.* 225 (2013) 734–743.
- [16] M. Nischk, P. Mazierski, M. Gazda, A. Zaleska, *Appl. Catal. B Environ.* 144 (2014) 674–685.
- [17] X. Qian, D. Qin, Q. Song, Y. Bai, T. Li, X. Tang, E. Wang, S. Dong, *Thin Solid Films* 385 (2001) 152–161.
- [18] H. Huang, D.Y. Leung, *ACS Catal.* 1 (2011) 348–354.
- [19] P.D. Cozzoli, R. Comparelli, E. Fanizza, M.L. Curri, A. Agostiano, D. Laub, *J. Am. Chem. Soc.* 126 (2004) 3868–3879.
- [20] A.L. Patterson, *Phys. Rev.* 56 (1939) 978–982.
- [21] R.A. Spurr, H. Myers, *Anal. Chem.* 29 (1957) 760–762.
- [22] K. Madhusudan Reddy, S.V. Manorama, A. Ramachandra Reddy, *Mater. Chem. Phys.* 78 (2003) 239–245.
- [23] Q. Xian, J. Yu, P.K. Wong, *J. Colloid Interface Sci.* 357 (2011) 163–167.
- [24] K.-I. Ishibashi, A. Fujishima, T. Watanabe, K. Hashimoto, *Electrochem. Commun.* 2 (2000) 207–210.
- [25] G. Louit, S. Foley, J. Cabillic, H. Coffigny, F. Taran, A. Valleix, J.P. Renault, S. Pin, *Radiat. Phys. Chem.* 72 (2005) 119–124.
- [26] Y. Su, Y. Deng, Y. Du, *J. Mol. Catal. A Chem.* 373 (2013) 18–24.
- [27] M. Erol, T. Dikici, M. Toparli, E. Celik, *J. Alloys Compd.* 604 (2014) 66–72.
- [28] Y. Alivov, M. Pandikunta, S. Nikishin, Z.Y. Fan, *Nanotechnology* 20 (2009) 225602–225608.
- [29] Z. Su, L. Zhang, F. Jiang, M. Hong, *Prog. Nat. Sci. Mater. Interface* 23 (2013) 294–301.
- [30] W. Kim, T. Tachikawa, G.H. Moon, T. Majima, W. Choi, *Angew. Chem. Int. Ed.* 126 (2014) 14260–14265.
- [31] J.C. Cardoso, T.M. Lizier, M.V.B. Zanoni, *Appl. Catal. B Environ.* 99 (2010) 96–102.
- [32] R.I. Bickley, F.S. Stone, *J. Catal.* 31 (1973) 389–397.
- [33] M.A. Behnajady, N. Modirshahla, M. Shokri, H. Elham, A. Zeinenezhad, *J. Environ. Sci. Health. Part A* 43 (2008) 460–467.
- [34] C.C. Wang, Z. Zhang, J.Y. Ying, *Nanostruct. Mater.* 9 (1997) 583–586.
- [35] M. Altomare, M. Pozzi, M. Allietta, L.G. Bettini, E. Selli, *Appl. Catal. B Environ.* 136 (2013) 81–88.
- [36] D. Tekin, *Appl. Surf. Sci.* 318 (2014) 132–136.
- [37] Y.C. Chou, Y. Ku, *Chem. Eng. J.* 225 (2013) 734–743.
- [38] H.C. Liang, X.Z. Li, J. Hazard, *Materials* 162 (2009) 1415–1422.
- [39] O.K. Varghese, D. Gong, M. Paulose, C.A. Grimes, E.C. Dickey, *J. Mater. Res.* 18 (2003) 156–165.
- [40] G. Li, Z.Q. Liu, J. Lu, L. Wang, Z. Zhang, *Appl. Surf. Sci.* 255 (2009) 7323–7328.
- [41] J. Yu, B. Wang, *Appl. Catal. B Environ.* 94 (2010) 295–302.
- [42] H. Li, L. Cao, W. Liu, G. Su, B. Dong, *Ceram. Int.* 38 (2012) 5791–5797.
- [43] A. Jaroenworarluck, D. Regonini, C.R. Bowen, R. Stevens, *Appl. Surf. Sci.* 256 (2010) 2672–2679.
- [44] D. Regonini, A. Jaroenworarluck, R. Stevens, C.R. Bowen, *Surf. Interface Anal.* 42 (2010) 139–144.
- [45] R. Parra, M.S. Góes, M.S. Castro, E. Longo, P.R. Bueno, J.A. Varela, *Chem. Mater.* 20 (2007) 143–150.
- [46] F. Schlott, R. Ohser-Wiedemann, T. Jordan, G. Kreisel, *Thin Solid Films* 520 (2012) 2549–2553.
- [47] M.A. Behnajady, H. Eskandarloo, N. Modirshahla, M. Shokri, *Desalination* 278 (2011) 10–17.
- [48] D. Fang, Z. Luo, K. Huang, D.C. Lagoudas, *Appl. Surf. Sci.* 257 (2011) 6451–6461.
- [49] Y. Cheng, H. Sun, W. Jin, N. Xu, *Chem. Eng. J.* 128 (2007) 127–133.
- [50] T.-C. Pan, S.-H. Wang, Y.-S. Lai, J.-M. Jehng, S.-J. Huang, *Appl. Surf. Sci.* 296 (2014) 189–194.
- [51] X. Liu, Z. Liu, J. Lu, X. Wu, B. Xu, W. Chu, *Appl. Surf. Sci.* 288 (2014) 513–517.
- [52] Y. Zhang, G. Zhao, H. Shi, Y.-N. Zhang, W. Huang, X. Huang, Z. Wu, *Electrochim. Acta* 174 (2015) 93–101.
- [53] Z. Xu, J. Yu, G. Liu, *Electrochem. Commun.* 13 (2011) 1260–1263.
- [54] Z. Xu, J. Yu, *Nanoscale* 3 (2011) 3138–3144.
- [55] J. Yu, G. Dai, B. Huang, *J. Phys. Chem. C* 113 (2009) 16394–16401.
- [56] J.G. Schwitzgebel, H. Ekerdt, *J. Phys. Chem.* 99 (1995) 5633–5638.
- [57] S. Xiong, S. George, Z. Ji, S. Lin, H. Yu, R. Damoiseaux, B. France, K.W. Ng, S.C.J. Loo, *Arch. Toxicol.* 87 (2013) 99–109.
- [58] M. El-Kemary, H. El-Shamy, I. El-Mehasseb, *J. Lumin.* 130 (2010) 2327–2331.
- [59] Á. Veres, T. Ríca, L. Janovák, M. Dömök, N. Buzas, V. Zöllmer, T. Seemann, A. Richardt, I. Dékány, *Catal. Today* 181 (2012) 156–162.
- [60] A. Kubacka, M.L. Cerrada, C. Serrano, M. Fernández-García, M. Ferrer, M. Fernández-García, *J. Phys. Chem. C* 113 (2009) 9182–9190.
- [61] T.T.Y. Tan, C.K. Yip, D. Beydoun, R. Amal, *Chem. Eng. J.* 95 (2003) 179–186.
- [62] H.M. Coleman, K. Chiang, R. Amal, *Chem. Eng. J.* 113 (2005) 65–72.
- [63] M.A. Behnajady, H. Eskandarloo, J. Nanosci. Nanotechnol. 13 (2013) 548–553.
- [64] J. Ren, W. Wang, S. Sun, L. Zhang, *J. Chang. Appl. Catal. B Environ.* 92 (2009) 50–55.
- [65] J. Tian, Y. Sang, Z. Zhao, W. Zhou, D. Wang, X. Kang, H. Liu, J. Wang, S. Chen, H. Cai, H. Huang, *Small* 9 (2013) 3864–3872.
- [66] H. Eskandarloo, A. Badiei, M.A. Behnajady, G.M. Ziarani, *Ultrason. Sonochem.* 26 (2015) 281–292.
- [67] K.B. Dhanalakshmi, S. Latha, S. Anandan, P. Maruthamuthu, *Int. J. Hydrogen Energy* 26 (2001) 669–674.
- [68] L.Q. Jing, Z.L. Xu, X.J. Sun, J. Shang, W.M. Cai, *Appl. Surf. Sci.* 180 (2001) 308.
- [69] L. Zhang, Y. Yang, R. Fan, J. Yu, L. Li, *J. Mater. Chem. A* 1 (2013) 12066–12073.

- [70] J. Liqiang, W. Dejun, W. Baiqi, L. Shudan, X. Baifu, F. Honggang, S. Jiazhong, J. Mol. Catal. A Chem. 244 (2006) 193–200.
- [71] B.F. Xin, L.Q. Jing, Z.Y. Ren, B.Q. Wang, H.G. Fu, J. Phys. Chem. B 109 (2005) 2805.
- [72] Y. Han, D. Peng, Z. Xu, H. Wan, S. Zheng, D. Zhu, Chem. Commun. 49 (2013) 8350–8352.
- [73] J. Yu, J. Xiong, B. Cheng, S. Liu, Appl. Catal. B Environ. 60 (2005) 211–221.
- [74] S. Hoang, S.P. Berglund, N.T. Hahn, A.J. Bard, C.B. Mullins, J. Am. Chem. Soc. 134 (2012) 3659–3662.
- [75] X.Q. Qiu, M. Miyauchi, K. Sunada, M. Minoshima, M. Liu, Y. Lu, D. Li, Y. Shimodaira, Y. Hosogi, Y. Kuroda, K. Hashimoto, ACS Nano 6 (2012) 1609–1618.